17 (2025) 100500

Contents lists available at ScienceDirect

Carbon Capture Science & Technology

journal homepage: www.elsevier.com/locate/ccst

Full Length Article

Mechanistic elucidation of cascade CO_2 hydrogenation enabled by Cu–Fe interfaces and oxygen vacancies

Hyeonji Yeom, Yongseok Kim, Woosung Leem, Jongmin Park, Kyungsu Na *

Department of Chemistry, Chonnam National University, Gwangju 61186, Republic of Korea

ARTICLE INFO

Keywords:
CO_2 hydrogenation
FeK/$CuAl_2O_4$
Exsolution
Oxygen vacancy
Hydrogen spillover
Reaction mechanism

ABSTRACT

The direct hydrogenation of CO_2 using green hydrogen offers a sustainable route to produce carbon-neutral liquid hydrocarbons, emerging as a viable alternative to conventional naphtha cracking. Although Fe-based $CuAl_2O_4$ catalysts have been widely studied for CO_2 hydrogenation, the mechanistic role of hydrogen spillover across dynamic Cu–Fe and associated oxygen vacancies has remained elusive. Here, the structure of FeK/$CuAl_2O_4$ catalysts was systematically tailored by controlling the reduction temperature to elucidate the exsolution-driven restructuration of pristine catalyst structure and its influences on the catalytic performance. We investigated the reaction process using in-situ DRIFTS analysis, from which we for the first time observed a cascade mechanism activated by hydrogen spillover, revealing various elementary reaction steps: (i) preferential adsorption of CO_2 as carbonate species on oxygen vacancies created by Cu exsolution in $CuAl_2O_4$ lattice, (ii) effective formate-mediated reverse water–gas shift (RWGS) reaction via the hydrogen spillover from exsolved Cu, (iii) promoted Fischer–Tropsch synthesis (FTS) reaction on Fe_5C_2 formed by the facilitated Fe carburization at the exsolved Cu–Fe_3O_4 interfaces, (iv) rapid desorption of hydrocarbons produced via controlled carbon chain growth. This cooperative interaction enabled the selective production of C_{5-11} hydrocarbons, achieving the highest C_{5-11} productivity of 290.7 mL g_{cat}^{-1} h^{-1}, surpassing our previous work at a CO_2 conversion of 36.4%. These findings establish a quantitative structure–performance–mechanism relationship and offer design principles for selectivity control toward desired hydrocarbon ranges in multifunctional CO_2 hydrogenation catalysts.

1. Introduction

The global energy landscape is undergoing a transformative shift as the urgency to mitigate climate change and reduce carbon emissions. Much attention has been focused on research for replacing petrochemical-based naphtha processes with carbon-consuming chemical processes (Cheng et al., 2024; Kim et al., 2022, 2024; Kwon et al., 2023; Shezad et al., 2025; Wei et al., 2017; Wen et al., 2025; Yang et al., 2024; Ye et al., 2019; Zhang et al., 2021). Traditional production for the petroleum-based liquid hydrocarbons has been heavily relying on oil refinery, which is a major contributor to greenhouse gas emissions and faces the impending challenge of resource depletion (Morales et al., 2015; Wei et al., 2017). To address these issues, innovative approaches that not only curb CO_2 emissions but also provide sustainable energy solutions are required. The process of CO_2 hydrogenation, which hopefully utilizes green hydrogen, has the potential to revolutionize production of CO_2-derived liquid fuels (Cheng et al., 2024; Kim et al., 2022, 2024; Wei et al., 2017; Ye et al., 2019). This process offers a dual benefit: it decreases atmospheric CO_2 levels by using it as a feedstock and produces carbon-neutral liquid-phase hydrocarbons, thereby presenting a viable alternative to conventional fossil fuels.

To directly convert CO_2 into liquid-phase hydrocarbons, tandem catalysis is often employed. Two different mechanistic pathways are accessible depending on the intermediate species: the methanol-mediated route and the CO-mediated modified Fischer–Tropsch synthesis (MFTS) (Cheng et al., 2024; Elmhamdi and Khaleel, 2025; Wei et al., 2017; Ye et al., 2019). The latter offers enhanced activity and reduced CO selectivity, rendering it well-suited for the production of hydrocarbon fuels (Cheng et al., 2024; Wei et al., 2017; Ye et al., 2019). This approach entails the initial reduction of CO_2 to CO via the reverse water–gas shift (RWGS) reaction, followed by the hydrogenation of CO into hydrocarbons via the FTS reaction. K-promoted Fe-supported $CuAl_2O_4$ catalysts have been developed by the present authors as tandem catalysts for direct hydrogenative CO_2 conversion (Kim et al., 2022, 2024). The catalytic components including Cu^0, $CuAl_2O_4$, and Fe_3O_4 phases are all highly active for RWGS reaction and K is electronic

* Corresponding author.
E-mail address: kyungsu_na@chonnam.ac.kr (K. Na).

https://doi.org/10.1016/j.ccst.2025.100500
Received 23 July 2025; Received in revised form 27 August 2025; Accepted 28 August 2025
Available online 28 August 2025

promoter for enhancing CO_2 adsorption and carbon chain growth (Wen et al., 2025; Ye et al., 2019; Zhang et al., 2021). Their strong interaction was reported to achieve stable tandem conversion of CO_2 to C_{5+} hydrocarbons by way of CO as the intermediate species. However, the specific origin of the structural evolution and the structure–activity relationship have not been clarified. The control of selectivity by regulating carbon chain growth in C_{5+} hydrocarbons and mechanism of CO_2 hydrogenation also remains to be elucidated.

Exsolution is one of the restructuration processes wherein cations in the lattice of oxide crystal migrate to the oxide surface under reducing conditions (Eguchi et al., 2008; Han et al., 2019; Kang et al., 2024; Myung et al., 2016; Schrenk et al., 2022; Srifa et al., 2018; Tian et al., 2015; Wang et al., 2023; Xiao et al., 2022). It can also be used for preparing supported metal nanoparticles (NPs) catalysts due to its unique ability to produce highly dispersed, stable metal nanoparticles with the formation of strong metal–oxide interfaces (Carrillo et al., 2020; Han et al., 2019; Schrenk et al., 2022; Singh et al., 2020; Xiao et al., 2022). Consequently, these exsolved metal NPs have been demonstrated to be highly competent catalysts with exceptional catalytic performance in a wide range of applications (Carrillo et al., 2020; Han et al., 2019; Myung et al., 2016; Schrenk et al., 2022; Wang et al., 2023; Xiao et al., 2022). In spinel-based catalysts, many excellent catalytic performances of exsolved metal have also been reported (Eguchi et al., 2008; Kang et al., 2024; Srifa et al., 2018; Tian et al., 2015). It was found that well-dispersed metallic Ni species in spinel framework formed by exsolution during reduction treatment shows highly stable activity without sintering than Ni supported on γ-Al_2O_3 in palm oil deoxygenation to green diesel (Srifa et al., 2018). Kang et al. demonstrated over Cu-based spinel catalysts to retard Cu agglomeration via Cu exsolution from spinel lattice during the RWGS reaction, giving a maximum CO_2 conversion rate than supported CuO/γ-Al_2O_3 catalysts (Kang et al., 2024).

$CuAl_2O_4$ has emerged as a promising platform because it undergoes exsolution under reducing conditions, where Cu cations migrate from the lattice to the surface. The redistribution of the cation coordination by exsolution in disordered spinel structure, a combination of normal spinel with a $(A^{2+})(B^{3+})_2(O^{2-})_4$ formula and inverse spinel having a $(B^{3+})(A^{2+}B^{3+})(O^{2-})_4$ formula (Bahmanpour et al., 2020; Elmhamdi and Khaleel, 2025; Zhao et al., 2017), has been reported to affect the environment of oxygen species in the metal oxide lattices (Kang et al., 2024; Tian et al., 2015). This restructuration produces highly dispersed metallic Cu and simultaneously generates oxygen vacancies in the spinel framework, both of which play crucial roles in CO_2 activation and RWGS kinetics, thereby influencing hydrocarbon chain growth in the subsequent FTS step. Despite these insights, the relationship among reduction temperature, exsolution behavior, oxygen vacancy formation, and their collective influence on CO_2 hydrogenation performance, particularly in the production of liquid hydrocarbons via the MFTS pathway, has not yet been fully clarified.

For successful CO_2 hydrogenation to produce liquid-phase high molecular-weight hydrocarbons, multiple catalytic components should make synergistic plays for CO_2 adsorption, H_2 activation, RWGS reaction, and FTS reaction in a balanced and harmonic manner. Herein, we realized this using FeK/$CuAl_2O_4$ wherein the location and proximity of multiple catalytic components and their relative concentrations on the external surface of $CuAl_2O_4$ were controlled via reduction temperature-dependent exsolution process. The systematic restructuration via controlled reduction temperature built the optimized catalyst architecture showing the balanced behaviors for CO_2 adsorption, H_2 activation, RWGS reaction and FTS reaction. By combining comprehensive characterization (in-situ XRD, XPS, TEM, in-situ DRIFTS), we construct a temperature–structure–function map that links Cu exsolution features to liquid hydrocarbon production. By revealing this correlation, our study provides a practical design lever for engineering exsolution-based catalysts and contributes to the development of scalable routes for CO_2–to–liquids conversion.

2. Experimental section

2.1. Catalyst preparation

2.1.1. Synthesis of $CuAl_2O_4$

The $CuAl_2O_4$ (abbreviated as CAO) was synthesized using a co-precipitation method. In a typical procedure, 0.032 mol (6.48 g) of aluminum isopropoxide (>98 %, Sigma Aldrich) was dissolved in 40.0 g of isopropyl alcohol in a round-bottomed flask, and the resultant solution was heated on a hot plate under reflux and stirring at 80 °C for 2 h. Then, 10.0 mL of an aqueous solution of $Cu(NO_3)_2{\cdot}2{\cdot}5H_2O$ (0.016 mol, 3.69 g, 98 %, Sigma Aldrich) was added dropwise to the flask, followed by further heating under reflux and stirring at 80 °C for 3 h. Upon cooling to room temperature, the solution was titrated with an aqueous solution of KOH (1 M) to adjust the pH to 9.5, and the resultant solution was stirred for an additional 3 h, resulting in the formation of a solid precipitate. The precipitate was filtered and subsequently dried in an oven at 100 °C for 12 h, then further subjected to calcination in a furnace at 800 °C for 4 h under an air flow (100 mL min^{-1}) to yield crystalline CAO.

2.1.2. Synthesis of FeK/CAO

The K-promoted Fe-supported on CAO (denoted as FeK/CAO) was prepared by a wet impregnation method using CAO as a support material. 1.0 g of CAO was suspended in 100.0 mL of deionized water within a round-bottomed glass flask. Then, 2.12 g of $Fe(NO_3)_3{\cdot}9H_2O$ (≥98 %, Sigma Aldrich) and 0.1 g of KNO_3 (99 %, Daejung) were added to the solution, and the mixtures were stirred for 1 hour at room temperature. After the excess water was evaporated at 70 °C, the mixtures were dried in an oven at 100 °C overnight. The resulting solid was then subjected to calcination in a furnace at 550 °C for 4 h under an air flow (100 mL min^{-1}) to yield FeK/CAO. A reduction treatment was performed at different temperatures. For the reduction, a flow of H_2 (60 mL min^{-1}) and Ar (50 mL min^{-1}) was applied for 4 h at 350, 400, 420, 450, and 500 °C, respectively. The reduced samples were denoted as FeK/CAO_X, wherein X is designated as the reduction temperature.

2.2. Materials characterization

Elemental contents were analyzed using inductively coupled plasma–optical emission spectroscopy (ICP–OES, Avio 550 Max instrument, PerkinElmer). X-ray diffraction (XRD) patterns were acquired using a Rigaku MiniFlex 600 apparatus equipped with Cu Kα radiation (λ = 0.1541 nm) at 600 W (40 kV, 15 mA). All XRD measurements were conducted under ambient conditions with a step size of 0.005°, a scanning rate of 1° min^{-1}, and a 2θ range spanning from 20 to 70° The phase compositions were determined using Rietveld refinement techniques through the Rigaku PDXL2 software package. N_2 physisorption analysis was conducted using a BELSORP MAX II volumetric analyzer. Prior to analysis, sample was degassed at 300 °C under vacuum for 3 h. N_2 physisorption analysis was then performed under a liquid nitrogen environment (77 K). The specific surface area and pore size were calculated according to the Brunauer–Emmett–Teller (BET) theory and Barrett–Joyner–Halenda (BJH) method, respectively.

H_2 temperature-programmed reduction (TPR) measurements were carried out employing a BEL-CAT analyzer (BEL, Japan) with a mass spectrometer (MS) detector. Prior to measurements, samples were degassed under a helium stream for 4 h at 400 °C in a quartz cell, followed by cooling to 50 °C. The TPR-MS process involved ramping the temperature from 50 to 1000 °C at a rate of 10 °C min^{-1} under H_2 flow. In-situ XRD spectra were obtained in H_2/N_2 gas condition with temperature-programmed heating mode using a Panalytical Empyrean XRD (Malvern Panalytical Ltd.). Transmission electron microscopy (TEM) images were obtained using a JEM-2100F (JEOL Ltd.) instrument operating at 200 kV. The elemental compositions were determined by energy dispersive spectroscopy (EDS) (X-Max 80T, Oxford Instruments

plc, UK). Sample preparation involved the use of a nickel grid to avoid interference from copper signals. X-ray photoelectron spectroscopy (XPS) analysis was conducted utilizing a K-ALPHA+ instrument (Thermo Fisher Scientific Inc.) equipped with a monochromatic Al Kα source connected to a 128-channel detector. Powder samples were affixed to a stainless-steel sample holder using carbon tape and analyzed under vacuum conditions of 5×10^{-9} mbar. Prior to the XPS analysis, all the samples were reduced under H_2 condition, sealed with vacuum to prevent exposure of the reduced sample to air. Gaussian−Lorentzian curve fitting was employed for spectral analysis of the Cu 2p, Al 2p, O 1 s, and Fe 2p regions after Shirley baseline correction, using the C 1 s peak (284.8 eV) as a reference.

H_2 and CO_2 temperature-programmed desorption (TPD) measurements were performed using the same BEL-CAT analyzer with a mass spectrometer (MS) detector. Prior to measurements, samples were reduced under a 5 % H_2/Ar stream for 4 h at different temperatures in a quartz cell, followed by cooling to 50 °C with helium purge to remove residual H_2. H_2 or CO_2 adsorption occurred using a 5 % H_2/He or 5 % CO_2/He flow over 1 h. After purging the cell with helium for 30 min, the TPD-MS process involved increasing the temperature from 50 to 1000 °C at a rate of 10 °C min^{-1} under helium flow.

2.3. Catalytic reaction studies

The catalytic reaction was conducted in a continuous flow fixed-bed microreactor with an inner diameter of 10.0 mm, which was equipped with a thermocouple positioned at the center of the catalyst bed. The catalyst used was 0.5 g with 20–40 mesh particles. A gas mixture consisting of CO_2, H_2, and Ar (in a volumetric ratio of 21:63:16) was pressurized to 3.0 MPa and the reaction was conducted at 320 °C in a gas hourly space velocity (GHSV) of 10,000 mL g_{cat}^{-1} h^{-1}. Ar was served as an internal standard gas. The effluent gases were analyzed using a gas chromatograph (GC, YL6500, YOUNG IN Chromass, Korea) equipped with both a thermal conductivity detector (TCD) and a flame ionization detector (FID) that were connected to a packed column (Supelco Analytical Metal packed GC column for TCD) and a capillary column (GS-GasPro for FID), respectively. Liquid products were collected as condensed using a cold trap (−4 °C) connected at the end of the reactor, and manually injected into the GC using a micro syringe for product analysis. The liquid products were analyzed with an FID connected to a capillary column (DB-5). The spent catalysts after the reaction were denoted as FeK/CAO_Xs.

CO_2 conversion and CO selectivity were determined on a molar carbon basis. The hydrocarbon distribution was computed using the total carbon moles, expressed in units of C-mol %, across all tested catalysts:

$$CO_2\ conversion\ (\%) = \frac{CO_{2,\ in} - CO_{2,\ out}}{CO_{2,\ in}} \times\ 100\%$$

where $CO_{2,in}$ and $CO_{2,out}$ are the moles of CO_2 fed to the reactor and exhausted from the reactor after the reaction, respectively.

$$CO\ selectivity\ (\%) = \frac{CO_{out}}{CO_{2,\ in} - CO_{2,\ out}} \times\ 100\%$$

where CO_{out} represents the moles of CO produced during the reaction and then exhausted from the reactor.

The distribution of individual hydrocarbon (C_i, i is the carbon number in hydrocarbon) in total hydrocarbons was given according to

$$C_i\ hydrocarbon\ distribution\ (C-mol\%) = \frac{mol\ of\ C_i\ hydrocarbon \times i}{\sum_{i=1}^{n} mol\ of\ C_i\ hydrocarbon \times i} \times\ 100\%$$

The carbon balances for all the reactions were approximately 95 %. The $C_{5–11}$ productivity was determined according to

$$C_{5-11}\ productivity\left(mL\ g_{cat}^{-1}\ h^{-1}\right) = CO_{2,flow} \times \frac{X_{CO_2}}{100} \times \frac{S_{C_{5-11}}}{100}$$

where $CO_{2,flow}$ is the flow rate of CO_2 fed into the reactor per catalyst. X_{CO_2} and $S_{C_{5-11}}$ represent CO_2 conversion (%), and $C_{5–11}$ hydrocarbons selectivity (%) computed including CO, respectively.

2.4. In-situ diffuse reflectance infrared Fourier transform spectroscopy

In-situ diffuse reflectance infrared Fourier transform spectroscopy (DRIFTS) was carried out using a Nicolet iS50R spectrometer (Thermo Fisher Scientific Inc.), equipped with a mercury–cadmium–telluride (MCT) detector and an environmental chamber with a ZnSe window. Measurements were performed in the range of 4000–650 cm^{-1}, with 16 scans accumulated at a resolution of 4 cm^{-1}.

For the time-dependent sequential adsorption of CO_2 and H_2, the FeK/CAO was first pretreated under a H_2 stream at 350 °C and 450 °C for 1 hour, respectively, using an 10 % H_2/Ar gas at a flow rate of 10 mL min^{-1}, followed by N_2 purging for 30 min at the same flow rate. After reduction pretreatment, the temperature of the chamber was decreased to 320 °C at 0.1 MPa. The background spectrum was collected under N_2 flow, and then the gas was switched to 10 % CO_2/N_2 at a flow rate of 10 mL min^{-1} and maintained for 30 min. After N_2 purging for 30 min, the gas was switched to 10 % H_2/Ar at a flow rate of 10 mL min^{-1} for 30 min. Spectra were continuously scanned during the process to observe surface-adsorbed species.

For the CO_2 hydrogenation reaction, the FeK/CAO was pretreated with H_2 under the same conditions as described above, and then cooled to 100 °C under an N_2 flow of 10 mL min^{-1}. The gas was switched to a 21 % CO_2/63 % H_2/16 % Ar mixture, and the chamber was pressured to 3 MPa at a flow rate of 5 mL min^{-1}. The background spectrum was collected at 3 MPa and 100 °C. The temperature was then raised to the reaction temperature of 320 °C and held for 60 min. The IR spectra were monitored in real time to detect the signals of the reaction intermediates.

3. Results and discussion

3.1. Reduction temperature-dependent restructuration of the FeK/CAO

The structural changes of FeK/CAO, consisting of $CuAl_2O_4$, CuO, and Fe_2O_3 (Figs. S1–2 and Table S1) were investigated under reducing atmosphere in the presence of H_2 using in-situ XRD, while increasing the temperature from 25 °C to 600 °C (Fig. 1). The reducing behaviors of metal oxides in FeK/CAO sample could be monitored with changes in XRD peaks. As the temperature increased, some existing peaks gradually disappeared while new peaks gradually appeared. New diffraction peaks appeared at 2θ of 43.3° and 50.4° when the applied temperature exceeded 350 °C, which respectively corresponded to the (111) and (200) lattice planes of Cu^0 (green squares in Figs. 1b–c). The XRD peak intensity of CuO was maintained though Cu^0 peaks began to appear in the heatmap (Fig. 1c), proposing that Cu^{2+} was being exsolved from the $CuAl_2O_4$ oxides (Liu et al., 2023; Plyasova et al., 2000). The intensity of Cu^0 increased with increasing temperature. When the applied temperature exceeded 420 °C, the Fe_2O_3 phases started to be reduced as evidenced by the decrease in XRD peak intensity (red inverse triangle in Figs. 1b–c), while the XRD peaks of Fe_3O_4 began to emerge (skyblue triangle in Figs. 1b–c). The H_2-TPR revealed a distinct shift in the reduction peak of FeK/$CuAl_2O_4$ to lower temperatures compared to pristine Fe_2O_3 (Fig. S1c), indicating that hydrogen atoms dissociated from Cu° facilitated the reduction of adjacent Fe oxides via hydrogen spillover mechanism. As a result of the increased degree of reduction from Fe_2O_3 to Fe_3O_4, the Fe_2O_3 diffraction peaks disappeared completely at 450 °C. These results demonstrated that Cu^{2+} was more reducible than Fe-oxides and hydrogen spillover from Cu^0 promoted the

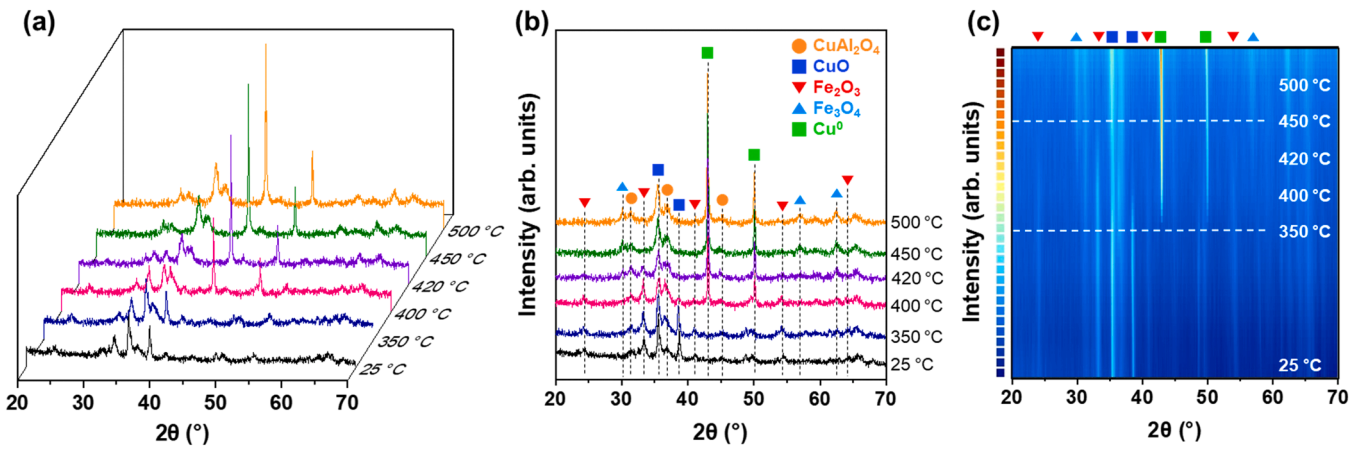

Fig. 1. (a,b) In-situ XRD patterns and (c) their corresponding heatmap showing the reduction temperature-dependent restructuration of the FeK/CAO catalyst measured under H_2/N_2 gas condition while increasing the temperature from 25 °C to 600 °C.

reduction of Fe_2O_3, which was consistent with the H_2-TPR results comparing Fe_2O_3 and $CuAl_2O_4$ in Fig. S1c. It also supported the expectation that the phase composition of FeK/CAO would change dramatically between 350 °C and 500 °C in the H_2-TPR profile, showing that the structure of CAO and the reduction degree of Fe-oxides were changed depending on the reduction temperature.

Fig. 2 shows TEM images with low magnification (Figs. 2a–e) and their corresponding STEM–EDS mapping images (Figs. 2f–j) obtained after H_2 reduction of the as-synthesized FeK/CAO at 350, 400, 420, 450, and 500 °C, respectively. The TEM images clearly showed the gradual temperature-dependent reconstruction of FeK/CAO upon H_2 reduction. The area and size of dense black domain in Figs. 2a–e increased as the reduction temperature increased, indicating that the thermal aggregation of metal oxide crystals became severe. The STEM–EDS mapping images disclosed the gradual temperature-dependent changes of surface elemental compositions (Figs. 2f–j, Table 1, and Table S2). As indicated by H_2-TPR and in-situ XRD results, Cu^{2+} was more reducible than Fe-oxides. Therefore, the reduction of Cu^{2+} species than Fe-oxides species was pronounced up to the reduction temperature of 400 °C and hence FeK/CAO_400 had the highest Cu/Al wt % ratio on its surface (Table 1). However, as the reduction temperature increased further, Fe-oxides species started to be reduced and hence external Fe concentration increased more significantly with gradual decrease of external Cu concentration until the reduction temperature reached 450 °C (Table S2).

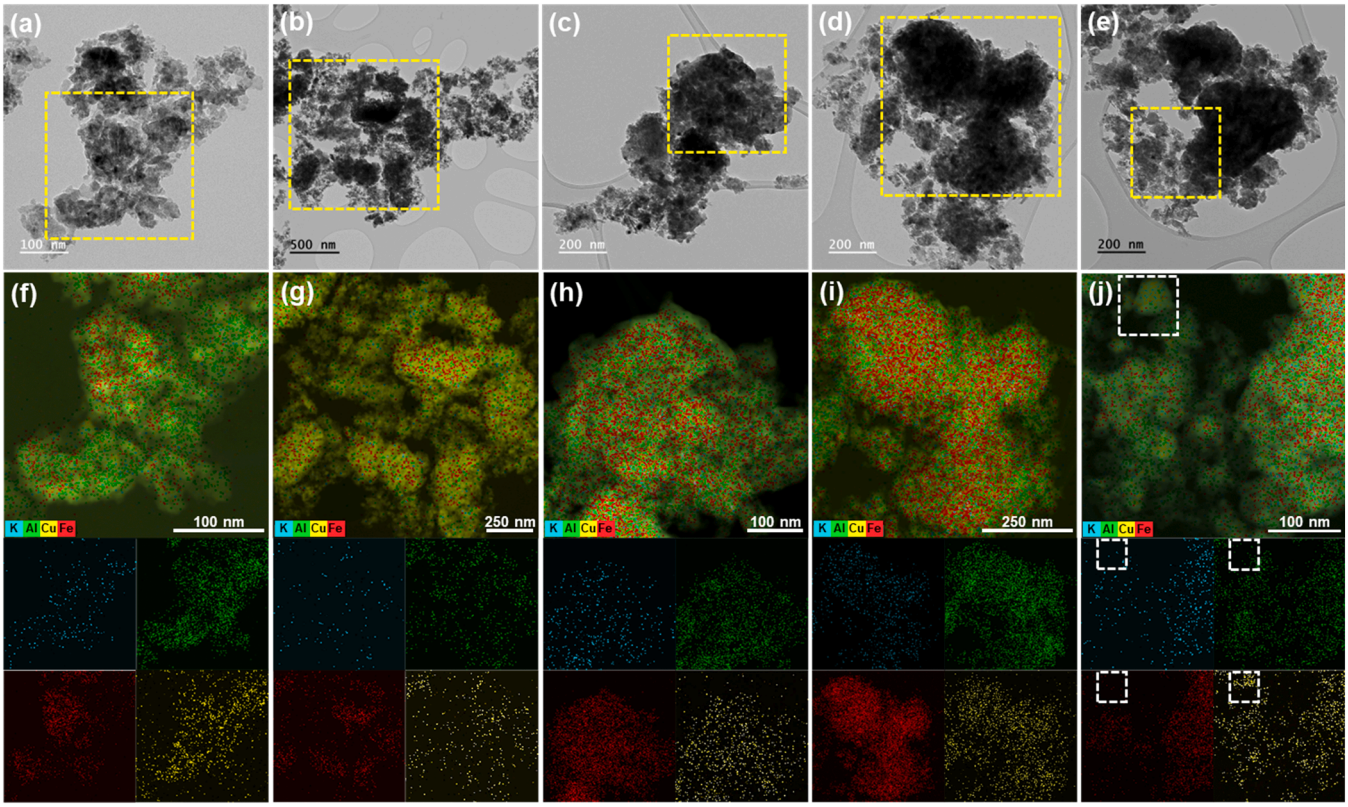

Fig. 2. (a–e) TEM images and (f–j) STEM–EDS mapping images of FeK/CAO catalysts reduced at different reduction temperatures. (a,f) FeK/CAO_350, (b,g) FeK/CAO_400, (c,h) FeK/CAO_420, (d,i) FeK/CAO_450, and (e,j) FeK/CAO_500. STEM–EDS mapping images are collected from the square boxes with yellow dashed lines in TEM images. HR-TEM images of the square box with white dashed lines in (j) are shown in Fig. S3.

Table 1
Surface elemental properties of as-synthesized FeK/CAO and reduced FeK/CAO catalysts.

Sample	FeK/CAO_assyn	FeK/CAO_350	FeK/CAO_400	FeK/CAO_420	FeK/CAO_450	FeK/CAO_500
Cu/Al[a]	0.59	0.64	0.77	0.58	0.60	0.70
Cu/Fe[a]	0.51	0.68	0.37	0.16	0.15	0.37
$Cu^{+}\&Cu^{0}$/($Cu^{2+}+Cu^{+}\&Cu^{0}$)[b]	0.06	0.17	0.61	0.49	0.39	0.41
(Cu_o^{2+}/Cu_t^{2+})[b]	0.92	1.00	1.54	2.13	2.42	3.07
(Al_o^{3+}/Al_t^{3+})[b]	1.13	1.16	1.16	1.26	1.54	2.96
O_V/($O_V+O_{Fe-O}+O_{CAO}$)[b]	0.41[c]	0.41	0.42	0.47	1.01	1.29
Fe^{2+}/($Fe^{3+}+Fe^{2+}+Fe^{0}$)[b]	0.59	0.61	0.66	0.74	0.77	0.70

[a] Surface elemental ratio derived from STEM−EDS mapping in Fig. 2 and Table S2.
[b] Area ratio determined from XPS results in Fig. 3 and Fig. S4.
[c] $O_V/(O_{OH}+O_V+O_{Fe-O}+O_{CAO})$.

This might be attributed to that the exsolved Cu° formed bimetallic crystals with Fe species as the reduction temperature increased, and hence the surface concentration of Cu decreased.

Within the bimetallic structure, the dissociated hydrogen atoms generated from Cu° could readily migrate to Fe species by hydrogen spillover, increasing the reduction degree of Fe oxides (Kim et al., 2024; Zheng et al., 2023). Therefore, as the reduction temperature increased to 450 °C, the Cu/Fe wt % ratio decreased because the concentration of external Fe increased (Table 1). Similarly, the Cu/Al wt % ratio decreased because the Cu species on the surface were covered by the Fe species due to the formation of bimetallic crystals between Cu^0 and Fe_3O_4. In FeK/CAO_500, on the other hand, the Cu metal was completely released from the $CuAl_2O_4$ (Fig. 2j and Fig. S3), resulting in a rebounding of external concentration of Cu^0 and hence an increase in both the Cu/Al and Cu/Fe wt % ratios again.

The changes in electronic structure of FeK/CAO upon reduction at different temperatures were investigated by XPS (Fig. 3). In general, $CuAl_2O_4$ could be synthesized as a mixed lattice having both normal and inverse spinel characteristics (Bahmanpour et al., 2020; Liu et al., 2023; Severino et al., 1998). Therefore, both Cu^{2+} in the Cu 2p XPS spectrum and Al^{3+} in the Al 2p XPS spectrum could be deconvoluted to both octahedral and tetrahedral sites (Figs. 3a–b, Figs. S4a–b, Table S3, and Table S4) (Bahmanpour et al., 2020; Severino et al., 1998). It is generally accepted that the low-coordinated Cu_t^{2+} in the spinel structure can be more easily reduced than the high-coordinated Cu_o^{2+} (Hong et al., 2023; Liu et al., 2023; Plyasova et al., 2000; Severino et al., 1998; Strohmeier et al., 1985; Xia et al., 1999). Indeed, as the reduction temperature increased, the Cu_o^{2+}/Cu_t^{2+} area ratio in the Cu 2p spectra increased, due to the higher reducibility of Cu_t^{2+} than Cu_o^{2+} (Fig. 3a, Fig. S4a, and Table 1). The $Cu^{+}\&Cu^{0}/(Cu_t^{2+}+Cu_o^{2+}+Cu^{+}\&Cu^{0})$ ratio was changed dramatically, in which the ratio reached a maximum of 0.61 when the reduction was carried out at 400 °C due to the exsolved metallic Cu^0 species (Table 1). However, the ratio decreased with increasing reduction temperature. This was because Fe species started to be reduced at higher reduction temperature, by which Cu was covered by Fe_3O_4 through the formation of bimetallic Cu and Fe. In FeK/CAO_500, however, the surface Cu^0 ratio increased again as significant amount of Cu metal was liberated from $CuAl_2O_4$ framework, which was in consistent with the trends in the Cu/Al wt % ratio on the surface of the reduced samples obtained from the STEM–EDS mapping (Fig. 2j and Table 1).

Similar to the higher reducibility of Cu_t^{2+} than Cu_o^{2+}, Al_t^{3+} was more reducible than Al_o^{3+}, resulting in a gradual temperature-dependent increase of Al_o^{3+}/Al_t^{3+} ratio as evidenced by Al 2p XPS spectra (Fig. 3b, Fig. S4b, and Table 1). The O 1 s XPS spectrum elucidated three different types of oxygen sites: lattice oxygen for $CuAl_2O_4$ (O_{CAO}) at 529.0 eV, lattice oxygen for Fe oxides (O_{Fe-O}) at 530.0 eV, and adsorbed oxygen species in oxygen vacancies (O_V) at 531.0 eV (Ponmudi et al., 2019; Zhu et al., 2023). As the reduction of Cu_t^{2+} increased, the amount of O_V increased proportionally as confirmed in O 1 s XPS spectra (Fig. 3c, Fig. S4c, and Table 1). The $O_V/(O_V+O_{Fe-O}+O_{CAO})$ ratio increased gradually from 0.41 in FeK/CAO_350 to 1.29 in FeK/CAO_500 (Table 1). This was related with the defect formation on the spinel framework created by the exsolved or released Cu metal (Plyasova et al., 2000). Therefore, more oxygen vacancies were formed by the increasing defect structure when the reduction temperature increased.

As the reduction degree of Fe oxides increased from the reduction temperature of 400 °C, a Fe^0 peak appeared in Fe 2p XPS spectra at 706.5 eV (Fig. 3d, Fig. S4d, Table 1, and Table S4) (Lei et al., 2018). The $Fe^{2+}/(Fe^{3+}+Fe^{2+}+Fe^{0})$ ratio increased with increasing reduction temperature due to reduction from Fe_2O_3 to Fe_3O_4 and/or FeO (Yang et al., 2021), with the highest ratio in FeK/CAO_450 (Table 1). In FeK/CAO_420 and FeK/CAO_450, charge transfer from Cu to Fe species in the bimetallic structure resulted in a lower shift in the binding energy of Fe^{2+} (Table S4). Conversely, the binding energy of $Cu^{+}\&Cu^{0}$ was shifted higher. The low $Cu^{+}\&Cu^{0}/(Cu_t^{2+}+Cu_o^{2+}+Cu^{+}\&Cu^{0})$ ratio also indicated that the Cu species were transferring electrons to assist in the reduction of Fe^{3+} to Fe^{2+} (Yang et al., 2021). Thus, in agreement with the in-situ XRD and STEM–EDS mapping results, increasing the reduction temperature increased the reduction degree of Fe oxides, which was attributed to hydrogen spillover in the bimetallic structure of exsolved Cu^0 and Fe species.

3.2. *Impact of structural evolution of the FeK/CAO on CO_2 hydrogenation*

Fig. 4a shows the reaction results showing the CO_2 conversion with CO selectivity for 48 h of time-on-stream (TOS) using the series of FeK/CAO catalysts reduced at five different reduction temperatures, and the averaged reaction results including the hydrocarbon distribution was graphitized in Fig. 4b As the reduction temperature increased, CO_2 conversion increased with gradual decrease of CO selectivity. The FeK/CAO_350 catalyst possessed the smallest amount of Cu^0 and hence H_2 dissociation was not sufficient, which activated the RWGS reaction on the spinel surfaces to produce CO dominantly with suppressing the CO hydrogenation (Fig. 4 and Table 2) (Bahmanpour et al., 2020). However, when the reduction temperature increased to 400 °C, i.e., FeK/CAO_400, larger amount of Cu^0 on the catalyst surface promoted H_2 dissociation, which in turn promoted CO hydrogenation. This led to higher CO_2 conversion, lower CO selectivity, and higher C_{5-11} hydrocarbons selectivity with productivity than FeK/CAO_350 (Figs. 4b–c and Table 2). The catalytic performance was further promoted as the reduction temperature increased to 420 and 450 °C. For FeK/CAO_420 and FeK/CAO_450, which have low Cu/Fe and high $Fe^{2+}/(Fe^{3+}+Fe^{2+}+Fe^{0})$ ratios on the surface (Fig. 4c), the bimetallic states of Cu^0 and Fe_3O_4 enhanced the RWGS reaction. The CO produced on Fe_3O_4 and Cu^0 as the active sites for the RWGS reactions promoted the carburization of Fe oxides, resulting in the formation of Fe carbides as the active sites of the FTS reaction (Boreriboon et al., 2018; Hwang et al., 2019; Yang et al., 2021). The Fe carbides facilitated C–C coupling and CO hydrogenation, resulting in decreased CO selectivity, increased CO_2 conversion, and C_{5-11} productivity.

Such synergistic plays of multiple catalytic components such as Cu^0, Fe_3O_4, and Fe carbides on $CuAl_2O_4$ surface were further increased for FeK/CAO_450 catalyst, resulting in the highest CO_2 conversion and C_{5-11} productivity (Fig. 4 and Table 2). This was attributed to the enhanced adsorption and activation of CO_2 in the rich oxygen vacancies created by the exsolution of Cu from $CuAl_2O_4$ lattice, where the activated CO_2 consecutively participated in the RWGS reaction followed by the FTS reaction at the bimetallic sites of Cu^0 and Fe_3O_4. Consequently, the catalytic performance of FeK/CAO_450 suggested that the balanced synergistic interplays among oxygen vacancies, Cu^0, Fe_3O_4, and Fe carbides were crucial for the production of C_{5-11} hydrocarbons via the

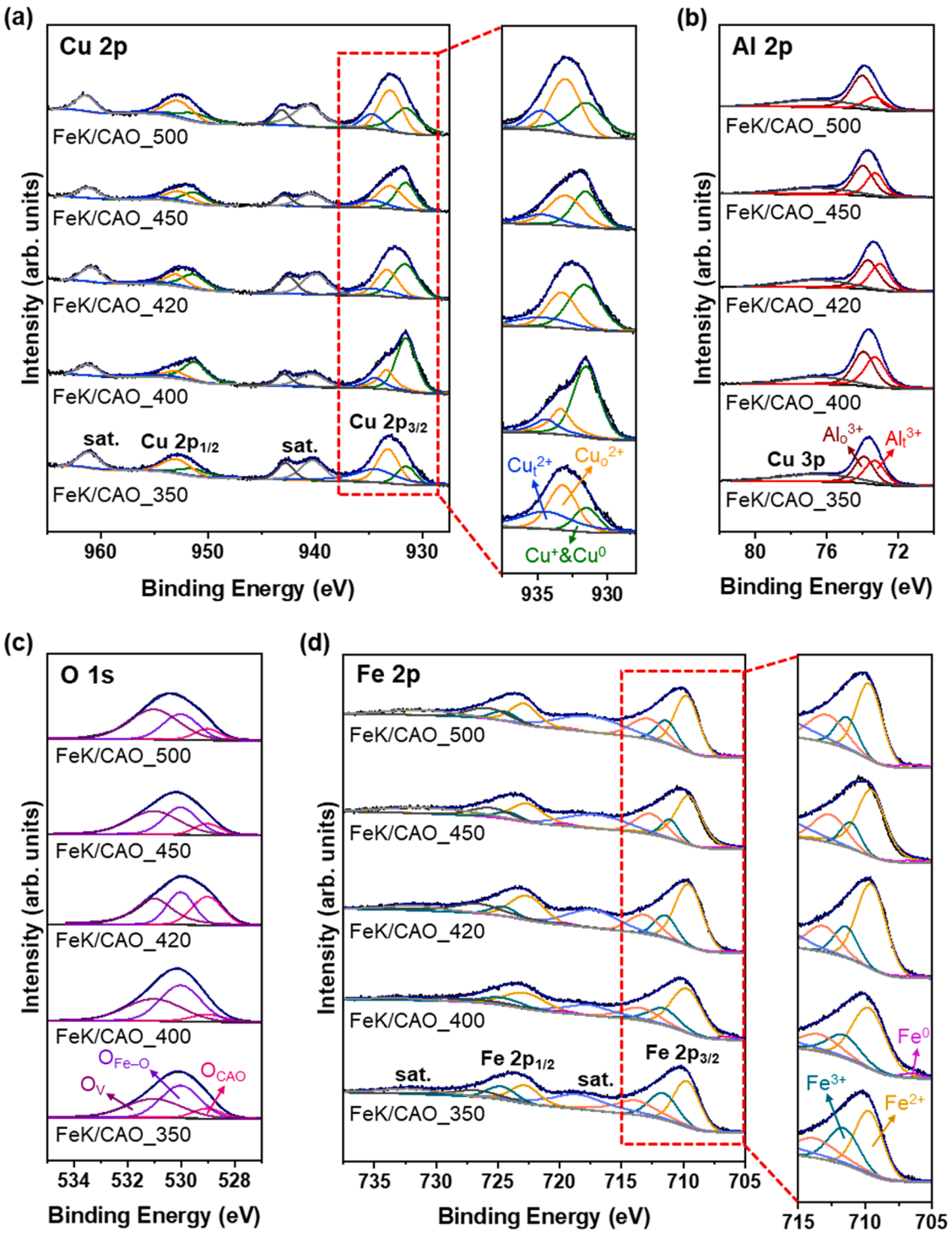

Fig. 3. XPS spectra showing (a) Cu 2p, (b) Al 2p, (c) O 1 s, and (d) Fe 2p regions of FeK/CAO catalysts reduced at different reduction temperatures.

direct hydrogenative conversion of CO_2. In FeK/CAO_500, however, the reduction temperature was too high, resulting in the release of Cu from the $CuAl_2O_4$ structure and the sintering of Cu metal (Fig. 2j and Fig. S3), which interfered balanced catalytic interplays and thereby significantly decreased the activation of CO_2 and H_2 as evidenced by CO_2 and H_2-TPD (Fig. 5 and Table S5), resulting in the decreased CO_2 hydrogenation activity. The distribution of the hydrocarbons produced after the reaction revealed that the α value became smaller as the reduction temperature increased (Fig. S5). This could be attributed to carbon chain growth being suppressed by the increased dissociation of H_2 from Cu^0, resulting in a gradual increase in short-chain hydrocarbons (Kattel et al., 2016; Wang et al., 2011; Wei et al., 2017). Thus, as the reduction temperature increased, the distribution for C_{12+} hydrocarbons decreased (Fig. 4b and Table 2).

3.3. *Adsorption behaviors for CO_2 and H_2 on different FeK/CAO structures*

Depending on the reduction temperatures, the CO_2 and H_2 adsorption behaviors on the FeK/CAO samples could be changed (Fig. 5 and

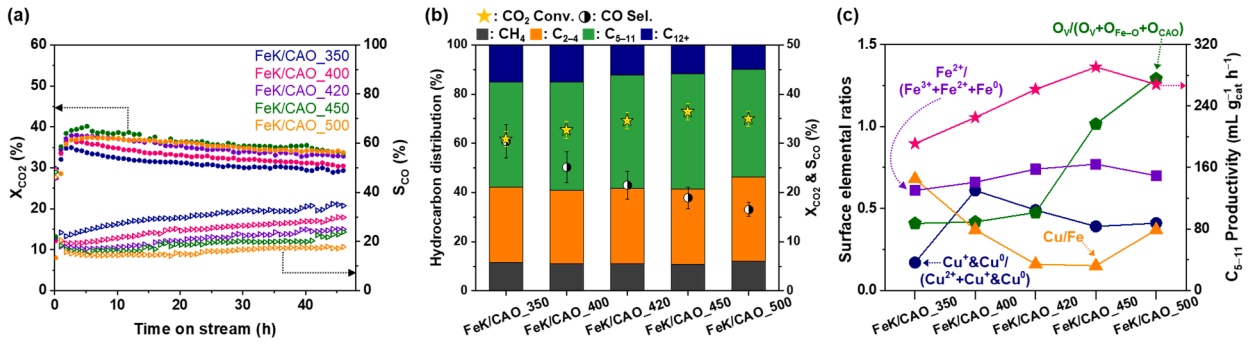

Fig. 4. (a) Reaction profiles showing CO_2 conversion (X_{CO2}, left y-axis) and CO selectivity (S_{CO}, right y-axis) during CO_2 hydrogenation for 48 h using FeK/CAO catalysts reduced at different reduction temperatures and (b) their averaged reaction data showing hydrocarbon distribution (left y-axis) (Reaction conditions: 320 °C, 3.0 MPa, $H_2/CO_2 = 3$, GHSV = 10,000 mL g_{cat}^{-1} h^{-1}). (c) Correlation between the surface elemental ratios (left y-axis) of FeK/CAO catalysts reduced at different reduction temperatures obtained from Table 1 and $C_{5–11}$ productivity (right y-axis) determined from (b).

Table 2
Summary of the reaction results of FeK/CAO catalysts obtained from Figs. 4a–b.

Sample	X_{CO2}	S_{CO}	Hydrocarbon distribution				$C_{5–11}$ productivity (mL g_{cat}^{-1} h^{-1})
			CH_4	$C_{2–4}$	$C_{5–11}$	C_{12+}	
FeK/CAO_350	30.8	30.5	11.5	30.7	42.5	15.3	191.0
FeK/CAO_400	32.6	25.3	11.1	29.9	44.0	15.0	225.0
FeK/CAO_420	34.5	21.5	10.9	30.8	46.0	12.2	261.6
FeK/CAO_450	36.4	18.9	10.7	30.6	46.9	11.8	290.7
FeK/CAO_500	34.9	16.5	12.1	34.1	43.8	10.0	268.0

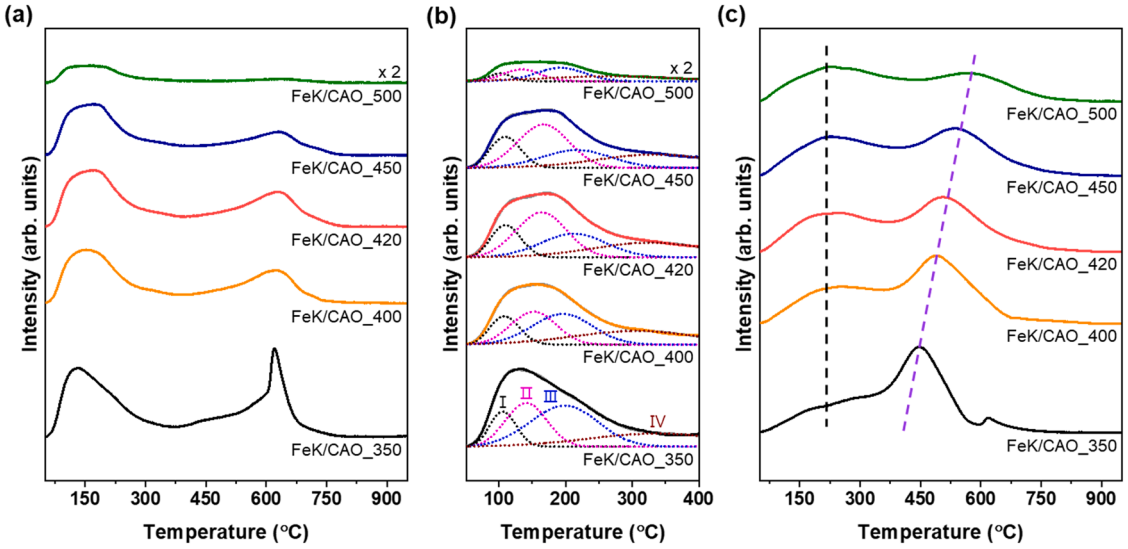

Fig. 5. (a) CO_2-TPD profiles, (b) its magnified profiles in the temperature range of 50–400 °C with four deconvoluted peaks designated as I, II, III, and IV, and (c) H_2-TPD profiles of FeK/CAO catalysts reduced at different reduction temperatures.

Table S5). The CO_2-TPD profiles could be divided into desorption peaks at 50–400 °C and at 400–950 °C (Fig. 5a), originating from the desorption of weakly physisorbed CO_2 and strongly chemisorbed CO_2, respectively (Khan et al., 2020). The lower temperature range (50–400 °C) could be further subdivided into four desorption peaks. First, peak I could be ascribed to the CO_2 desorption from Cu–O and Al–O pairs of $CuAl_2O_4$ (Trueba et al., 2005). The FeK/CAO_350 had the largest number of CO_2 adsorption sites with 0.532 mmol g^{-1} (Table S5) due to the lower thermal aggregation of the metal oxide crystals, which preserved the pristine mesoporous structure of FeK/CAO (Fig. 2a). As the reduction temperature increased, the thermal agglomeration of the metal oxides became severe and the mesoporous structure was gradually collapsed (Figs. 2b–e), resulting in the decrease of CO_2 adsorption. Second, peaks II and III could be originated from the CO_2 desorption from oxygen vacancies on the CAO surface (Jiang et al., 2025; Liu et al., 2018), and the amount of adsorbed CO_2 gradually increased with increasing oxygen vacancies (Table 1 and Fig. 5b), with the largest amount of 0.133 mmol g^{-1} in FeK/CAO_450 (Table S5). Third, peak IV could be originated from the CO_2 desorption from adsorbed CO_2 on potassium (Boreriboon et al., 2018; Montanari et al., 2011), and the amount of adsorbed CO_2 gradually decreased as the potassium was covered by exsolved Cu and reduced Fe species with increasing reduction temperature (Table S5).

The higher temperature range (400–950 °C) could be attributed to the CO_2 desorption from Fe_2O_3 having strong CO_2 adsorption strength (Fig. 5a) (Hakim et al., 2016). With increasing the reduction

temperature, the Fe_2O_3 was gradually reduced to Fe_3O_4 (Figs. 1–3). It is generally known that the Fe_3O_4 has lower CO_2 adsorption sites than Fe_2O_3 (Hakim et al., 2016), and therefore the amount of adsorbed CO_2 detected at higher temperature range (400–950 °C) decreased as the reduction temperature increased (Table S5). For the FeK/CAO_500 sample, the amount of CO_2 adsorption sites decreased dramatically, which could be attributed to the formation of large particle size of Cu metal with decrease of interparticle mesoporosity (Fig. 2j and Fig. S3), and the high reduction degree of Fe oxides as indicated by XPS (Fig. 3d).

Like the CO_2-TPD, the H_2-TPD profiles could be divided into two desorption peaks at 50–350 °C and 350–950 °C (Fig. 5c), deriving from the desorption of H_2 species with weak and strong strengths, respectively. The weak adsorption sites could be attributed to the hydrogen chemisorbed by Cu species and the hydrogen spilled from adsorbed on Cu species to oxygen vacancies on the support surface (Ai et al., 2018; Ni et al., 2019; Yang et al., 2019; Zheng et al., 2023). In FeK/CAO_350, the H_2 adsorption at lower temperature was less due to lower surface concentrations of Cu^0 and oxygen vacancies (Fig. 5c and Table S5). However, with increasing reduction temperature, Cu^0 gradually formed bimetallic structure with Fe species, thereby the electron transfer from Cu^0 to Fe oxides became prominent, which promoted the adsorption of H_2 on the Cu^0. At the same time, due to the increased hydrogen spillover of adsorbed H_2 into the oxygen vacancies, the amount of H_2 adsorption at lower temperatures gradually increased as the reduction temperature increased (black dashed line in Fig. 5c). Contrary to the weak adsorption sites at lower temperatures of 50–350 °C, the peak at higher temperatures of 350–950 °C could be originated mostly from the strong adsorption of H_2 on Fe oxides (Ning et al., 2019). As the reduction temperature increased, the amount of H_2 adsorption became progressively smaller due to the increased reduction degree of Fe oxides, as evidenced by in-situ XRD, STEM–EDS mapping, and XPS results (Figs. 1–3). This caused the increase of adsorption strength of H_2, and hence the H_2 desorption peak was shifted to a higher temperature (purple dashed line in Fig. 5c).

3.4. Unraveling the synergy effect of controlled structure of the FeK/CAO

To unravel the key active sites and their synergistic plays for the production of liquid-phase $C_{5–11}$ hydrocarbons through CO_2 hydrogenation, spent FeK/CAO catalysts after 48 h of reaction were analyzed using XRD (Fig. S6 and Table S6), TEM (Fig. S7), STEM–EDS mapping (Fig. S8), and XPS (Fig. S9 and Table S7). The XRD pattern and HR-TEM image of FeK/CAO_350s distinguished the exsolved Cu^0 species that made interfaces with neighboring metal oxides by reactant H_2 during reaction (Fig. S6 and Fig. S7f). Fe carbides were observed in all the spent FeK/CAO catalysts as confirmed by XRD, TEM, STEM–EDS mapping images, and Fe 2p XPS spectra (Figs. S6–9). The Fe carbides were coated by carbon layer, forming a core@shell structure (Figs. S7f–j). According to the Rietveld refinement of XRD (Fig. S6 and Table S6) and Fe 2p XPS (Fig. S9 and Table S7), the concentration of Fe carbides (Fe_3C+Fe_5C_2) was the highest in FeK/CAO_450s. The concentration of Cu^0 was remarkably the highest in FeK/CAO_500s (Fig. S6 and Table S6), which confirmed that the severe release of Cu species from $CuAl_2O_4$ as confirmed by the STEM–EDS mapping image showing the sintering of Cu metal (yellow dots in Fig. S8e).

It should be noted that the control of reduction temperature changed various structural properties: (i) the degree of Cu exsolution from $CuAl_2O_4$, (ii) the oxygen vacancies, (iii) the bimetallic structure of Cu and Fe, (iv) the degree of reduction of Fe species. At a reduction temperature of 450 °C, the controlled FeK/CAO structure had a large number of weak CO_2 adsorption sites (0.231 mmol g^{-1}) and a small number of strong CO_2 adsorption sites (0.126 mmol g^{-1}) due to increased oxygen vacancies and Fe_3O_4, respectively (Figs. 5a–b and Table S5). These weak CO_2 adsorption sites promoted CO_2 activation and the strong CO_2 adsorption sites induced less C–C coupling, resulting in selective production of $C_{5–11}$ hydrocarbons (Khan et al., 2020; Nasriddinov et al., 2022). The balanced basicity favored the adsorption of CO_2 and also facilitated the formation of iron carbides through CO_2 dissociation (Boreriboon et al., 2018; Jiang et al., 2020; Nasriddinov et al., 2022). Therefore, the formation of Fe carbides was favored more in FeK/CAO_450 (Figs. S6–9, and Tables S6–7). In terms of H_2 activation, FeK/CAO_450 also had many weak H_2 chemisorption sites (0.142 mmol g^{-1}) due to Cu^0 and oxygen vacancies and few strong H_2 chemisorption sites (0.167 mmol g^{-1}) due to Fe_3O_4 (Fig. 5c and Table S5). The optimal concentration of Fe carbides and the H_2 chemisorption sites with optimal strengths might improve the FTS performance (Han et al., 2020). Consequently, the FeK/CAO reduced at 450 °C led to effective CO_2 and H_2 activation, accelerated Fe carburization, and controlled carbon chain growth.

From the comprehensive characterizations relating with reaction results, the contribution of a synergistic play of multiple catalytic components of FeK/CAO on the CO_2 hydrogenation was schematized. Scheme 1 depicted the structural evolution of the FeK/CAO catalyst before (state I) and after the reductive treatment at 450 °C under H_2 condition (state II), as well as during the CO_2 hydrogenation (state III), with corresponding representative TEM images, suggesting catalytic interplays for production of hydrocarbons. The reduction treatment at 450 °C under H_2 condition induced remarkable structural evolution on FeK/CAO (state II in Scheme 1): (i) Cu was exsolved from $CuAl_2O_4$ lattice with formation of strong metal–support interaction between Cu^0 and $CuAl_2O_4$, (ii) the exsolution of Cu remained oxygen vacancies on the $CuAl_2O_4$ surface, (iii) the exsolved Cu° formed bimetallic structure with Fe_3O_4 that was reduced from Fe_2O_3 via hydrogen spillover of dissociated hydrogen atoms from Cu^0. Therefore, the abundant oxygen vacancies and bimetallic states of Cu^0 and Fe_3O_4 on FeK/CAO_450 enhanced the CO_2 adsorption and its hydrogenative conversion to CO via the RWGS reaction (state III in Scheme 1). The accelerated CO generation promoted the carburization of Fe species, by which Fe_5C_2 were formed. It facilitated carbon bond growth and hydrogenation of CO, resulting in $C_{5–11}$ hydrocarbons productivity superior to previously published work (Table S8).

3.5. Mechanism study using in-situ drifts

To study the reaction processes, FeK/CAO_350 and FeK/CAO_450 catalysts with different degrees of exsolution and thus showing different reaction results were investigated using in-situ DRIFTS under two different analyses conditions. As the first analysis condition, these catalysts were applied to the sequential activation processes of CO_2 and H_2, where the feed gases of 10 % CO_2/N_2, N_2, and 10 % H_2/Ar were sequentially provided at 320 °C under ambient pressure for 30 min each, while the catalyst surface was monitored by IR at 5-min intervals (Figs. 6a–b).

When a CO_2 flow was applied, both FeK/CAO_350 and FeK/CAO_450 initially exhibited broad peaks in the ranges of 1280–1390 and 1510–1635 cm^{-1} due to the symmetric and asymmetric O–C–O stretching vibrations of carboxylate ($CO_2^{\delta-}$) species adsorbed on the catalyst surface, respectively (Figs. 6a–b and Table S9). During the CO_2 feeding for 30 min, initially evolved IR peaks of carboxylate species were maintained on FeK/CAO_350 without significant changes (Fig. 6a), but striking changes were observed on FeK/CAO_450 (Fig. 6b). In FeK/CAO_450, after 20 min, carbonate (CO_3*) species at 1065 and 1506 cm^{-1}, bicarbonate (HCO_3*) species at 1420 and 1637 cm^{-1}, and formate (HCOO*) species at 1272 cm^{-1} appeared while the IR peaks of carboxylate species were broadened to be disappeared (Fig. 6b), indicating that the CO_2 activation on FeK/CAO_450 was more dynamic than FeK/CAO_350. It should be reminded that FeK/CAO_450 exhibited a high H_2 activation capability due to the exsolved Cu^0 as characterized by H_2-TPD (Fig. 5c and Table S5). Therefore, hydrogen atoms dissociated and adsorbed on exsolved Cu^0 during the H_2 reduction process would assist the formation of bicarbonate and formate species during CO_2 activation on FeK/CAO_450. Conversely, in the case of FeK/CAO_350, the

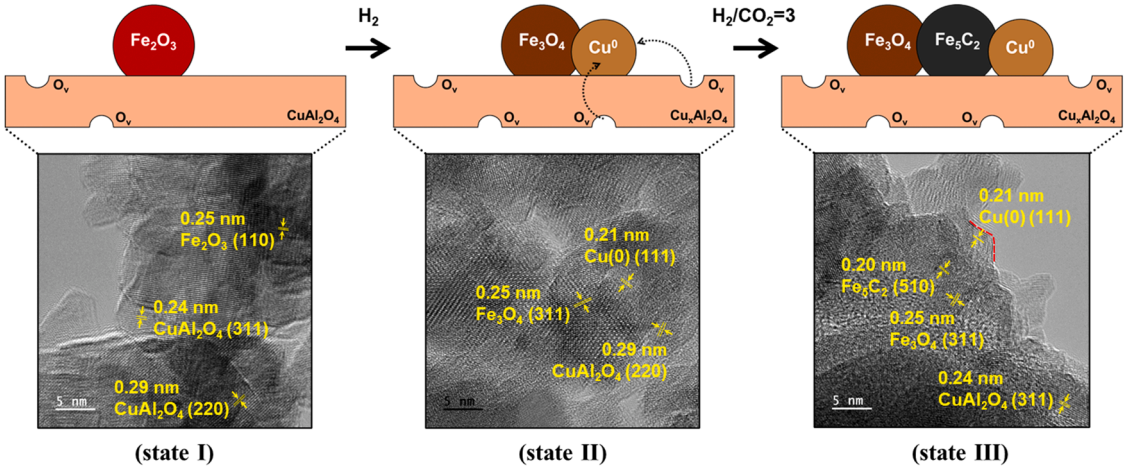

Scheme 1. Schematic representation of the structural evolution in the FeK/CAO catalyst before (state I) and after the reductive treatment at 450 °C under H_2 condition (state II), as well as during the CO_2 hydrogenation (state III) with corresponding HR-TEM images.

concentration of exsolved Cu^0 was significantly lower, and the activated hydrogen atoms were also deficient, resulting in the inefficient activation of initially activated carboxylate species.

Furthermore, the abundant oxygen vacancies and CO_2 adsorption capacity of FeK/CAO_450 as characterized by CO_2-TPD (Figs. 5a–b and Table S5) might further enhance the adsorption of carbonate species (Lu et al., 2024). As the duration of CO_2 feeding increased, the intensities of carbonate, bicarbonate, and formate species gradually increased (Fig. 6b and Fig. S10). Even after switching to N_2 flow, these intensities remained almost unchanged. After switching to H_2 gas, an intense peak evolved at 2021 cm^{-1}, which is attributed to the formation of CO* adsorbed on Cu^0 surface. This could suggest that Cu° facilitated H_2 dissociation, and the spillover of dissociated hydrogen atoms induced the decomposition of various activated species (e.g., carbonate, bicarbonate, and formate species) as their IR peaks disappeared during H_2 feeding (Fig. 6b). As the duration of H_2 feeding increased, the intensity of the CO* peak gradually increased, indicating that the CO* species became more concentrated on the catalyst surface.

In contrast, the carbonate, bicarbonate, and formate species were rarely detected on FeK/CAO_350 (Fig. 6a), attributable to the lower concentration of oxygen vacancies for enhanced CO_2 activation and the absence of exsolved Cu^0 for efficient H_2 activation. The first DRIFTS study with sequential activation processes of CO_2 and H_2 demonstrated that CO_2 adsorption as carbonate species favors at oxygen vacancies and that hydrogen spillover plays a decisive role in forming formate species and CO. In FeK/CAO_450, the cooperative interplay between oxygen vacancies and exsolved Cu^0 enabled the efficient generation of CO via the RWGS reaction.

As the second experimental condition, in-situ DRIFTS spectra were collected under the realistic reaction condition under mixed CO_2/H_2 gas flow at 3 MPa at 320 °C for 60 min. Both FeK/CAO_350 and FeK/CAO_450 catalysts formed CO from CO_2 via formate-mediated RWGS reaction, as indicated by the appearance of broad and intense IR peaks at 2180 and 2111 cm^{-1} corresponding to gaseous CO in the analysis chamber (Figs. 6c–d and Table S9). In addition, they produced olefins probably via CO-mediated FTS reaction, as indicated by the appearance of IR peaks at 1645 and 1635 cm^{-1} originating from olefinic species (Figs. 6c–d and Table S9). In a broad point of view, it seems like that both catalysts made olefin products via CO-mediated FTS reaction. However, the concentrations of adsorbed species on both catalysts are remarkably different, as shown in the contour map of DRIFTS spectra of FeK/CAO_350 and FeK/CAO_450 (Fig. S11) and DRIFTS spectra with different y-axis scales (0.03 of Fig. 6c vs. 0.01 of Fig. 6d). This indicates that the concentration of adsorbed species on FeK/CAO_350 is much higher than that on FeK/CAO_450, suggesting that the detailed reaction processes would be different.

In FeK/CAO_350, which contained Fe_2O_3 and $CuAl_2O_4$ with low oxygen vacancies ratio (Fig. 1, Fig. 3c, and Table 1), CO_2 was adsorbed as carbonate species on $CuAl_2O_4$ and then converted to bidentate species by H_2, subsequently forming formate species and surface hydroxyl groups (Scheme 2a). The formate species were then decomposed by H_2 to generate CO and H_2O. The IR peaks at 3670 and 3650 cm^{-1} corresponding to surface hydroxyl groups (OH*) became pronounced from 200 °C, and the IR peaks of gaseous CO signals at 2180 and 2111 cm^{-1} appeared rapidly from 300 °C (Fig. 6c). The peaks of carbonate (1653/1540/1507/1456 cm^{-1}), bidentate (1716/1699/1473 cm^{-1}), and formate (1559/1521 cm^{-1}) species also observed at 300 °C. Due to the deficiency of FTS active sites such as Fe_5C_2 (Fig. S6 and Table S6), the generated CO was converted dominantly to CH_4, resulting in the initial appearance of IR peak at 3015 cm^{-1} corresponding to a gaseous CH_4 instead of IR peaks of olefins at 1645 and 1635 cm^{-1}. The interpretation of DRIFTS is consistent with that the FeK/CAO_350 showed the lowest CO_2 conversion and C_{5-11} hydrocarbons productivity, and the highest CO selectivity (Fig. 4 and Table 2).

However, in FeK/CAO_450, which contained Cu^0, Fe_3O_4, and $CuAl_2O_4$ with high oxygen vacancies ratio (Fig. 1, Fig. 3c, and Table 1), CO_2 was adsorbed as carbonate species at oxygen vacancies, and hydrogen atoms dissociated on exsolved Cu^0 spilled over, promoting the formation of bicarbonate (Scheme 2b), consistent with the result in Fig. 6b The bicarbonate-derived formate species then decomposed to CO, while further hydrogen spillover facilitated H_2O formation. The RWGS reaction was also accelerated on Fe_3O_4, and the resultant CO could be rapidly dissociated, promoting Fe carburization with the formation of Fe_3C and subsequently Fe_5C_2 between Cu^0 and Fe_3O_4 (Fig. S6 and Table S6). The resulting Fe_5C_2 facilitated the CO-FTS reaction that effectively produced olefins (Scheme 2b). Since CO intermediates was efficiently utilized in Fe_5C_2 formation and the FTS reaction, FeK/CAO_450 showed less intense IR peak of gaseous CO than FeK/CAO_350 (Figs. 6c–d and Fig. S11). The IR peak of gaseous CH_4 also began to appear at 3015 cm^{-1} less intensively, later than FeK/CAO_350, implying that the conversion of CO to olefins was enhanced in FeK/CAO_450 with less CH_4 production. The less intense IR peaks of olefinic species on FeK/CAO_450 indicates that the olefins produced were promptly desorbed with shorter residence time than FeK/CAO_350. In contrast, FeK/CAO_350 with many strong CO_2 adsorption sites (Fig. 5a–b and Table S5), the delayed desorption of olefins could lead to more intense carbon chain growth resulting in higher C_{12+} hydrocarbons, whereas in FeK/CAO_450 with few strong CO_2 adsorption sites (Fig. 5a–b and Table S5), the rapid desorption of olefins after proper C–C coupling could promote higher C_{5-11} hydrocarbons (Fig. 4b, Fig. S5a, and

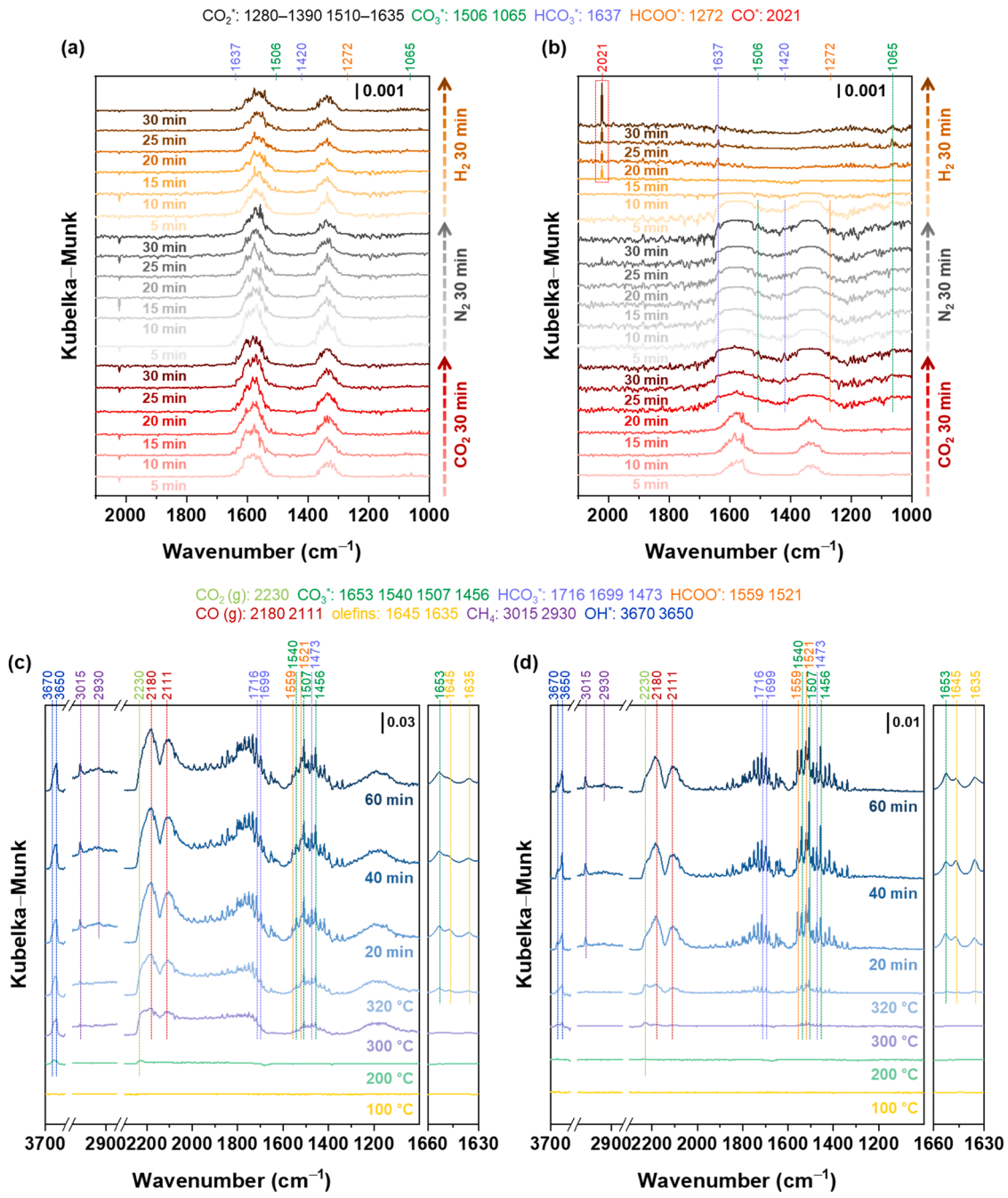

Fig. 6. Ambient pressure in-situ DRIFTS spectra obtained by switching the feed gas from 10 % CO_2/N_2 to N_2, followed by 10 % H_2/Ar at 320 °C for (a) FeK/CAO_350 and (b) FeK/CAO_450. High pressure in-situ DRIFTS spectra obtained under reaction conditions of CO_2:H_2=1:3, 320 °C, and 3 MPa for (c) FeK/CAO_350 and (d) FeK/CAO_450.

Table 2).

4. Conclusions

Exsolution-driven restructuration of FeK/$CuAl_2O_4$ catalysts demonstrated a promising strategy for enhancing CO_2 hydrogenation toward liquid-phase $C_{5–11}$ hydrocarbons. By tuning the reduction temperature, the structural evolution of the catalyst was precisely regulated, enabling an optimal interplay between exsolved Cu^0, Fe_3O_4, Fe_5C_2, and oxygen vacancies. These structural modifications facilitated key reaction steps, including CO_2 activation, hydrogen spillover, the reverse water–gas shift (RWGS) reaction, and subsequent Fischer–Tropsch synthesis (FTS). The optimized catalyst, FeK/$CuAl_2O_4$ reduced at 450 °C, exhibited the highest CO_2 conversion and $C_{5–11}$ hydrocarbons productivity due to the synergistic effect of Cu^0–Fe_3O_4 bimetallic sites and oxygen vacancy-enriched surfaces. In-depth mechanistic studies, including in-situ DRIFTS, elucidated that the preferential adsorption of CO_2 at oxygen vacancies, followed by formate-mediated RWGS, significantly contributed to enhanced CO generation and its subsequent hydrogenation. The cooperative interactions between exsolved Cu^0 and Fe_3O_4 facilitated Fe carburization, forming catalytically active Fe_5C_2 species that promoted selective C–C coupling and hydrocarbon growth. Furthermore, the rapid desorption of hydrocarbons from the catalyst surface prevented excessive carbon chain elongation, ensuring high selectivity for the $C_{5–11}$ hydrocarbons. This work highlights the pivotal role of catalyst restructuring in governing reaction pathways and represents the potential of

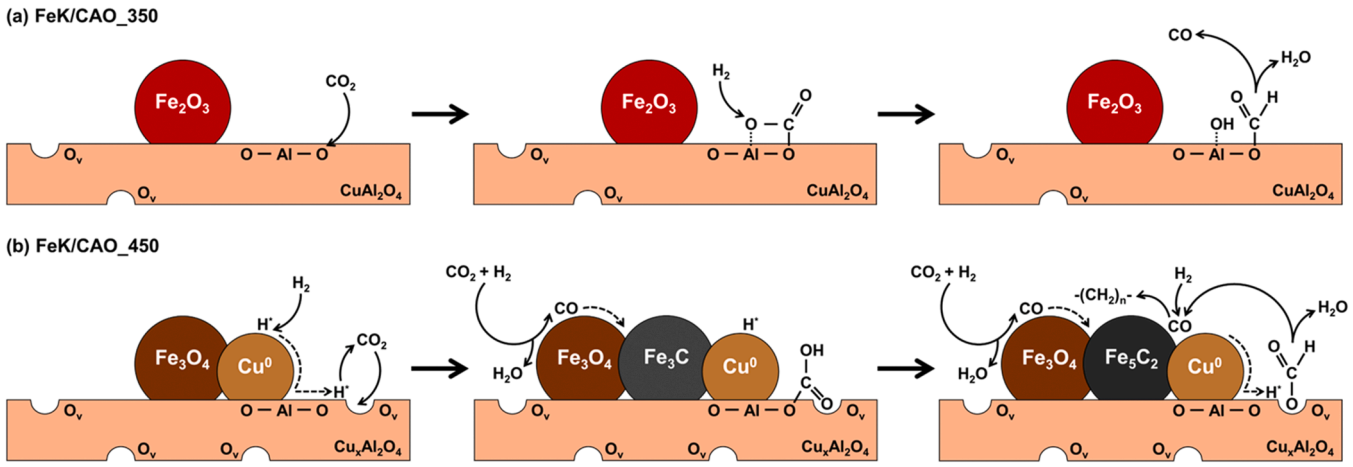

Scheme 2. Schematic representations showing reaction mechanisms of CO_2 hydrogenation to hydrocarbons over (a) FeK/CAO_350 and (b) FeK/CAO_450.

exsolution engineering for developing next-generation catalysts for CO_2 hydrogenation. The findings not only provide a fundamental understanding of the structure–activity relationship in Fe-based tandem catalysts but also offer a scalable approach for producing carbon-neutral chemicals.

CRediT authorship contribution statement

Hyeonji Yeom: Writing – review & editing, Writing – original draft, Investigation, Data curation. **Yongseok Kim:** Investigation, Data curation, Writing – review & editing. **Woosung Leem:** Investigation, Data curation. **Jongmin Park:** Investigation, Data curation. **Kyungsu Na:** Writing – review & editing, Writing – original draft, Supervision, Project administration, Investigation, Funding acquisition, Data curation, Conceptualization.

Declaration of competing interest

The authors declare that they have no known competing financial interests or personal relationships that could have appeared to influence the work reported in this paper.

Acknowledgements

This work was supported by the National Research Foundation of Korea (NRF) grant funded by Korea government (MSIT) (RS-2024-00349276 and RS-2024-00466475), and by the Global-Learning & Academic research institution for Master's·PhD students, and Postdocs (LAMP) Program of the NRF grant funded by the Ministry of Education (RS-2024-00442775). The authors are grateful to the Center of Research Facilities at the Chonnam National University for their assistance in the TEM, XPS, and ICP–OES analyses.

Data availability

All data are available in the main text or the supplementary materials.

Supplementary materials

Supplementary material associated with this article can be found, in the online version, at doi:10.1016/j.ccst.2025.100500.

References

Ai, P., Tan, M., Reubroycharoen, P., Wang, Y., Feng, X., Liu, G., Yang, G., Tsubaki, N., 2018. Probing the promotional roles of cerium in the structure and performance of Cu/SiO_2 catalysts for ethanol production. Catal. Sci. Technol. 8, 6441–6451. https://doi.org/10.1039/c8cy02093k.

Bahmanpour, A.M., Héroguel, F., Kılıç, M., Baranowski, C.J., Schouwink, P., Röthlisberger, U., Luterbacher, J.S., Kröcher, O., 2020. Essential role of oxygen vacancies of Cu-Al and Co-Al spinel oxides in their catalytic activity for the reverse water gas shift reaction. Appl. Catal. B Environ. 266, 118669. https://doi.org/10.1016/j.apcatb.2020.118669.

Boreriboon, N., Jiang, X., Song, C., Prasassarakich, P., 2018. Higher hydrocarbons synthesis from CO_2 hydrogenation over K-and La-promoted Fe–Cu/TiO_2 catalysts. Top. Catal. 61, 1551–1562. https://doi.org/10.1007/s11244-018-1023-1.

Carrillo, A.J., Kim, K.J., Hood, Z.D., Bork, A.H., Rupp, J.L.M., 2020. $La_{0.6}Sr_{0.4}Cr_{0.8}Co_{0.2}O_3$ perovskite decorated with exsolved Co nanoparticles for stable CO_2 splitting and syngas production. ACS Appl. Energy. Mater. 3, 4569–4579. https://doi.org/10.1021/acsaem.0c00249.

Cheng, K., Li, Y., Kang, J., Zhang, Q., Wang, Y., 2024. Selectivity control by relay catalysis in CO and CO_2 hydrogenation to multicarbon compounds. Acc. Chem. Res. 57, 714–725. https://doi.org/10.1021/acs.accounts.3c00734.

Eguchi, K., Shimoda, N., Faungnawakij, K., Matsui, T., Kikuchi, R., Kawashima, S., 2008. Transmission electron microscopic observation on reduction process of copper-iron spinel catalyst for steam reforming of dimethyl ether. Appl. Catal. B Environ. 80, 156–167. https://doi.org/10.1016/j.apcatb.2007.11.020.

Elmhamdi, A., Khaleel, M., 2025. Recent innovations in spinel oxide-based catalysts for CO_2 hydrogenation to olefins. Carbon Capture Sci. Technol. 14, 100367. https://doi.org/10.1016/j.ccst.2025.100367.

Hakim, A., Marliza, T.S., Abu Tahari, N.M., Wan Isahak, R.W.N., Yusop, R.M., Mohamed Hisham, W.M., Yarmo, A.M., 2016. Studies on CO_2 adsorption and desorption properties from various types of iron oxides (FeO, Fe_2O_3, and Fe_3O_4). Ind. Eng. Chem. Res. 55, 7888–7897. https://doi.org/10.1021/acs.iecr.5b04091.

Han, H., Park, J., Nam, S.Y., Kim, K.J., Choi, G.M., Parkin, S.S.P., Jang, H.M., Irvine, J.T. S., 2019. Lattice strain-enhanced exsolution of nanoparticles in thin films. Nat. Commun. 10, 1471. https://doi.org/10.1038/s41467-019-09395-4.

Han, Z., Qian, W., Zhang, H., Ma, H., Sun, Q., Ying, W., 2020. Effect of rare-earth promoters on precipitated iron-based catalysts for Fischer-Tropsch synthesis. Ind. Eng. Chem. Res. 59, 14598–14605. https://doi.org/10.1021/acs.iecr.9b06760.

Hong, Z., Jin, Y., Wang, S., Gao, Z., Huang, W., 2023. Enhanced catalytic stability of non-stoichiometric Cu–Al spinel catalysts for dimethyl ether synthesis from syngas: effect of coordination structure. Fuel Process. Technol. 247, 107772. https://doi.org/10.1016/j.fuproc.2023.107772.

Hwang, S.M., Han, S.J., Min, J.E., Park, H.G., Jun, K.W., Kim, S.K., 2019. Mechanistic insights into Cu and K promoted Fe-catalyzed production of liquid hydrocarbons via CO_2 hydrogenation. J. CO_2 Util. 34, 522–532. https://doi.org/10.1016/j.jcou.2019.08.004.

Jiang, J., Wen, C., Tian, Z., Wang, Y., Zhai, Y., Chen, L., Li, Y., Liu, Q., Wang, C., Ma, L., 2020. Manganese-promoted Fe_3O_4 microsphere for efficient conversion of CO_2 to light olefins. Ind. Eng. Chem. Res. 59, 2155–2162. https://doi.org/10.1021/acs.iecr.9b05342.

Jiang, X., Li, X., Xiong, S., Liu, W., Yan, J., Duan, X., Song, S., Cheng, Q., Tian, Y., Li, X., 2025. Synergistical effect of CoIn alloy and oxygen vacancies over Co-In-Zr ternary catalysts boosting CO_2 hydrogenation to methanol. Cabon Capture Sci. Technol. 14, 100376. https://doi.org/10.1016/j.ccst.2025.100376.

Kang, H.F., Liu, Y.J., Lu, Y., Zhang, P., Tang, M.X., Gao, Z.X., Ge, H., Fan, W.B., 2024. Exploring the sustained release catalysis of $CuAl_2O_4$ spinel for highly effective CO_2 conversion to CO. J. Catal. 432, 115427. https://doi.org/10.1016/j.jcat.2024.115427.

Kattel, S., Yu, W., Yang, X., Yan, B., Huang, Y., Wan, W., Liu, P., Chen, J.G., 2016. CO_2 hydrogenation over oxide-supported PtCo catalysts: the role of the oxide support in determining the product selectivity. Angew. Chem. Int. Ed. 128, 8100–8105. https://doi.org/10.1002/ange.201601661.

Khan, M.K., Butolia, P., Jo, H., Irshad, M., Han, D., Nam, K.W., Kim, J., 2020. Selective conversion of carbon dioxide into liquid hydrocarbons and long-chain α-olefins over

Fe-amorphous AlO_x bifunctional catalysts. ACS Catal 10, 10325–10338. https://doi.org/10.1021/acscatal.0c02611.
Kim, Y., Kim, Y., Yeom, H., Na, K., 2024. Consequence of controlled hydrogen spillover on FeK/$CuAl_2O_4$ in CO_2 hydrogenation. Chem. Eng. J. 493, 152614. https://doi.org/10.1016/j.cej.2024.152614.
Kim, Y., Song, Y., Kim, Y., Na, K., 2022. Multifunctional long-lived catalysts for direct hydrogenative conversion of CO_2 to liquid hydrocarbons with upscaling C_{5+} productivity. J. Mater. Chem. A 10, 21862–21873. https://doi.org/10.1039/d2ta05138a.
Kwon, S., Yang, H., Yu, Y., Choi, Y., Kim, N., Kim, G.H., Ko, K.C., Na, K., 2023. A sustainable carbon-consuming cycle based on sequential activation of CO_2 and CH_4 using metal oxides. Appl. Catal. B Environ. 339, 123120. https://doi.org/10.1016/j.apcatb.2023.123120.
Lei, Y., Jiang, J., Bi, T., Du, J., Pang, X., 2018. Tribological behavior of in situ fabricated graphene–nickel matrix composites. RSC Adv. 8, 22113. https://doi.org/10.1039/c8ra02510j.
Liu, B., Li, C., Zhang, G., Yao, X., Chuang, S.S.C., Li, Z., 2018. Oxygen vacancy promoting dimethyl carbonate synthesis from CO_2 and methanol over Zr-doped CeO_2 nanorods. ACS Catal. 8, 10446–10456. https://doi.org/10.1021/acscatal.8b00415.
Liu, Y.J., Kang, H.F., Hou, X.N., Qing, S.J., Zhang, L., Gao, Z.X., Xiang, H.W., 2023. Sustained release catalysis: dynamic copper releasing from stoichiometric spinel $CuAl_2O_4$ during methanol steam reforming. Appl. Catal. B Environ. 323, 122043. https://doi.org/10.1016/j.apcatb.2022.122043.
Lu, B., Wu, F., Li, X., Luo, C., Zhang, L., 2024. Reconstruction of interface oxygen vacancy for boosting CO_2 hydrogenation by Cu/CeO_2 catalysts with thermal treatment. Carbon Capture Sci. Technol. 10, 100173. https://doi.org/10.1016/j.ccst.2023.100173.
Montanari, T., Castoldi, L., Lietti, L., Busca, G., 2011. Basic catalysis and catalysis assisted by basicity: FT-IR and TPD characterization of potassium-doped alumina. Appl. Catal. A Gen. 400, 61–69. https://doi.org/10.1016/j.apcata.2011.04.016.
Morales, M., Gonzalez-García, S., Aroca, G., Moreira, M.T., 2015. Life cycle assessment of gasoline production and use in Chile. Sci. Total Environ. 505, 833–843. https://doi.org/10.1016/j.scitotenv.2014.10.067.
Myung, J.H., Neagu, D., Miller, D.N., Irvine, J.T.S., 2016. Switching on electrocatalytic activity in solid oxide cells. Nature 537, 528–531. https://doi.org/10.1038/nature19090.
Nasriddinov, K., Min, J.E., Park, H.G., Han, S.J., Chen, J., Jun, K.W., Kim, S.K., 2022. Effect of Co, Cu, and Zn on FeAlK catalysts in CO_2 hydrogenation to C_{5+} hydrocarbons. Catal. Sci. Technol. 12, 906–915. https://doi.org/10.1039/d1cy01980e.
Ni, J., Leng, W., Mao, J., Wang, J., Lin, J., Jiang, D., Li, X., 2019. Tuning electron density of metal nickel by support defects in Ni/ZrO_2 for selective hydrogenation of fatty acids to alkanes and alcohols. Appl. Catal. B Environ. 253, 170–178. https://doi.org/10.1016/j.apcatb.2019.04.043.
Ning, W., Li, B., Wang, B., Yang, X., Jin, Y., 2019. Enhanced production of C_{5+} hydrocarbons from CO_2 hydrogenation by the synergistic effects of Pd and K on γ-Fe_2O_3 catalyst. Catal. Lett. 149, 431–440. https://doi.org/10.1007/s10562-018-2622-y.
Plyasova, L.M., Yur'eva, T.M., Yu Molina, I., Kriger, T.A., Balagurov, A.M., Davydova, L. P., Zaikovskii, V.I., Kustova, G.N., Malakhov, V.V., Dovlitova, L.S., 2000. Dynamics of structural transformations in the reduction of copper aluminate. Kinet. Catal. 41, 429–436. https://doi.org/10.1007/BF027553832000.
Ponmudi, S., Sivakumar, R., Sanjeeviraja, C., Gopalakrishnan, C., Jeyadheepan, K., 2019. Facile fabrication of spinel structured n-type $CuAl_2O_4$ thin film with nanograss like morphology by sputtering technique. Appl. Surf. Sci. 483, 601–615. https://doi.org/10.1016/j.apsusc.2019.03.314.
Schrenk, F., Lindenthal, L., Drexler, H., Urban, G., Rameshan, R., Summerer, H., Berger, T., Ruh, T., Opitz, A.K., Rameshan, C., 2022. Impact of nanoparticle exsolution on dry reforming of methane: improving catalytic activity by reductive pre-treatment of perovskite-type catalysts. Appl. Catal. B Environ. 318, 121886. https://doi.org/10.1016/j.apcatb.2022.121886.
Severino, F., Brito, J.L., Laine, J., Fierro, J.L.G., López Agudo, A., 1998. Nature of copper active sites in the carbon monoxide oxidation on $CuAl_2O_4$ and $CuCr_2O_4$ spinel type catalysts. J. Catal. 177, 82–95. https://doi.org/10.1006/jcat.1998.2094.
Shezad, N., Safdar, M., Arellano-García, H., Tai, C.W., Chen, S., Seo, D.K., You, S., Vomiero, A., Akhtar, F., 2025. Deciphering the role of APTES in tuning the metal support interaction of NiO nanolayers over hierarchical zeolite 13X for CO_2 methanation. Carbon Capture Sci. Technol. 15, 100424. https://doi.org/10.1016/j.ccst.2025.100424.
Singh, B.K., Lee, S., Na, K., 2020. An overview on metal-related catalysts: metal oxides, nanoporous metals and supported metal nanoparticles on metal organic frameworks and zeolites. Rare Met. 39, 751–766. https://doi.org/10.1007/s12598-019-01205-6.
Srifa, A., Kaewmeesri, R., Fang, C., Itthibenchapong, V., Faungnawakij, K., 2018. $NiAl_2O_4$ spinel-type catalysts for deoxygenation of palm oil to green diesel. Chem. Eng. J. 345, 107–113. https://doi.org/10.1016/j.cej.2018.03.118.
Strohmeier, B.R., Leyden, D.E., Scott Field, R., Hercules, D.M., 1985. Surface spectroscopic characterization of $Cu/A1_2O_3$ catalysts. J. Catal. 94, 514–530. https://doi.org/10.1016/0021-9517(85)90216-7.
Tian, S., Wang, S., Wu, Y., Gao, J., Xie, H., Li, X., Yang, G., Han, Y., Tan, Y., 2015. The real active sites over Zn-Cr catalysts for direct synthesis of isobutanol from syngas: structure-activity relationship. RSC Adv 5, 89273–89281. https://doi.org/10.1039/c5ra17289f.
Trueba, M., Trasatti, S.P., 2005. γ-Alumina as a support for catalysts: a review of fundamental aspects. Eur. J. Inorg. Chem. 2005, 3393–3403. https://doi.org/10.1002/ejic.200500348.
Wang, W., Wang, S., Ma, X., Gong, J., 2011. Recent advances in catalytic hydrogenation of carbon dioxide. Chem. Soc. Rev. 40, 3703–3727. https://doi.org/10.1039/c1cs15008a.
Wang, Y., Gallego, J., Wang, W., Timmer, P., Ding, M., Luciano, A.S., Weber, T., Glatthaar, L., Guo, Y., 2023. Unveiling the self-activation of exsolved $LaFe_{0.9}Ru_{0.1}O_3$ perovskite during the catalytic total oxidation of propane. Chin. J. Catal. 54, 250–264. https://doi.org/10.1016/S1872-2067(23)64547-4.
Wei, J., Ge, Q., Yao, R., Wen, Z., Fang, C., Guo, L., Xu, H., Sun, J., 2017. Directly converting CO_2 into a gasoline fuel. Nat. Commun. 8, 15174. https://doi.org/10.1038/ncomms15174.
Wen, H., Liao, H., Pan, X., Sun, K., Jiang, J., Liao, Y., Yuan, X., Sun, H., 2025. Recent advances in carbon-based catalysts for CO_2 hydrogenation toward circular economy. Carbon Capture Sci. Technol. 16, 100482. https://doi.org/10.1016/j.ccst.2025.100482.
Xia, W.S., Wan, H.L., Chen, Y., 1999. Cluster model study on the surface interactions of γ-alumina-supported metal oxides. J. Mol. Catal. A Chem. 138, 185–195. https://doi.org/10.1016/S1381-1169(98)00145-9.
Xiao, Y., Xie, K., 2022. Active exsolved metal–oxide interfaces in porous single-crystalline ceria monoliths for efficient and durable CH_4/CO_2 reforming. Angew. Chem. Int. Ed. 61, e202113079. https://doi.org/10.1002/anie.202113079.
Yang, H., Kwon, S., Choi, Y., Jang, H., Leem, W., Heo, J.H., Kim, C., Song, T., Na, K., 2024. Unveiling the sequential CO_2/CH_4 activation process on Co_3O_4 nanoparticles encapsulated by mesoporous silica shell. Appl. Catal. B Environ. 357, 124304. https://doi.org/10.1016/j.apcatb.2024.124304.
Yang, L., Pastor-Pérez, L., Villora-Pico, J.J., Sepúlveda-Escribano, A., Tian, F., Zhu, M., Han, Y.F., Ramirez Reina, T., 2021. Highly active and selective multicomponent Fe-Cu/CeO_2-Al_2O_3 catalysts for CO_2 upgrading via RWGS: impact of Fe/Cu ratio. ACS Sustain. Chem. Eng. 9, 12155–12166. https://doi.org/10.1021/acssuschemeng.1c03551.
Yang, W., Yang, X., Jia, J., Hou, C., Gao, H., Mao, Y., Wang, C., Lin, J., Luo, X., 2019. Oxygen vacancies confined in ultrathin nickel oxide nanosheets for enhanced electrocatalytic methanol oxidation. Appl. Catal. B Environ. 244, 1096–1102. https://doi.org/10.1016/j.apcatb.2018.12.038.
Ye, R.P., Ding, J., Gong, W., Argyle, M.D., Zhong, Q., Wang, Y., Russell, C.K., Xu, Z., Russell, A.G., Li, Q., Fan, M., Yao, Y.G., 2019. CO_2 hydrogenation to high-value products via heterogeneous catalysis. Nat. Commun. 10, 5698. https://doi.org/10.1038/s41467-019-13638-9.
Zhang, P., Han, F., Yan, J., Qiao, X., Guan, Q., Li, W., 2021. N-doped ordered mesoporous carbon (N-OMC) confined Fe_3O_4-FeC_x heterojunction for efficient conversion of CO_2 to light olefins. Appl. Catal. B Environ. 299, 120639. https://doi.org/10.1016/j.apcatb.2021.120639.
Zhao, Q., Yan, Z., Chen, C., Chen, J., 2017. Spinels: controlled preparation, oxygen reduction/evolution reaction application, and beyond. Chem. Rev. 117, 10121–10211. https://doi.org/10.1021/acs.chemrev.7b00051.
Zheng, X., Yu, P., Liu, Y., Ma, Y., Cao, Y., Cai, Z., Zhou, L., Huang, K., Zheng, S., Jiang, L., 2023. Efficient hydrogenation of methyl palmitate to hexadecanol over Cu/m-ZrO_2 catalysts: synergistic effect of Cu species and oxygen vacancies. ACS Catal. 13, 2047–2060. https://doi.org/10.1021/acscatal.2c06151.
Zhu, W., Zuo, X., Zhang, X., Deng, X., Ding, D., Wang, C., Yan, J., Wang, X., Wang, G., 2023. MOFs-derived CuO–Fe_3O_4@C with abundant oxygen vacancies and strong Cu–Fe interaction for deep mineralization of bisphenol A. Environ. Res. 228, 115847. https://doi.org/10.1016/j.envres.2023.115847.